Manganese: The Oxygen-evolving Complex & Models

G. Charles Dismukes & Rogier T. van Willigen
Princeton University, Princeton, NJ, USA

Based in part on the article Manganese: Oxygen-Evolving Complex & Models by Lars-Erik Andréasson & Tore Vänngård which appeared in the Encyclopedia of Inorganic Chemistry, First Edition.

Abbreviations

PSII = Photosystem II; WOC = Water-oxidizing complex; OEC = Oxygen-evolving complex; (B)RC = (Bacterial) Reaction Center; Chl = Chlorophyll; Bchl = Bacteriochlorophyll; XRD = X-ray diffraction; EPR = Electron paramagnetic resonance; EXAFS = Extended X-ray absorption fine structure; ENDOR = Electron-nuclear double resonance; ESEEM = Electron spin echo envelope modulation; ($Tyr_Z = Y_Z$) = D1Tyr161; ATP = Adenosine Triphosphate; KIE = Kinetic isotope effect; UV = UltraViolet; (FT−)IR = (Fourier Transform) InfraRed.

1 INTRODUCTION: ORIGIN AND SIGNIFICANCE OF OXYGENIC PHOTOSYNTHESIS

The production of O_2 by the oxidation of water within photosynthetic organisms is a striking signature of life on Earth. This biological innovation appeared in the precursors to contemporary cyanobacteria circa 2.2–3.8 billion years ago and had profound global geological consequences.[1,2] Very little is known about how water splitting chemistry was invented.[3–5] By using water as an inexhaustible source of electrons and protons, it enabled the proliferation of phototrophic life everywhere on the planet. This event was nature's analog of the 'universal big bang'. It transformed the atmosphere from anaerobic to O_2-rich, perfused phototrophic life throughout the oceans, pigmented the surface of Earth in a carpet of green chlorophyll, and enabled the biogeochemical cycles to develop their present forms. The emergence of atmospheric O_2 permitted the development of respiratory metabolism with its vastly more efficient energy production. This new boost in metabolic energy *supercharged* the engine of life and led to all complex life as we know it.

O_2 is a by-product of splitting water into electrons and protons within a wide variety of photosynthetic organisms, including both prokaryotes (cyano- and oxyphoto-bacteria), and eukaryotes (green algae and higher plants). Water splitting is driven by the membrane pigment-protein complex known as the photosystem II–water oxidizing complex (PSII-WOC) or oxygen-evolving complex (PSII-OEC). The electrons and protons are ultimately used to store energy in the phospho-anhydride bond of ATP and to reduce CO_2 to carbohydrate, the precursors for synthesis of the biopolymers needed by the organism. Some cyanobacteria and green algae also use the protons and electrons to synthesize hydrogen under anaerobic conditions, presumably to eliminate excess reducing capacity.

A single class of PSII-WOC enzymes is found in all O_2-producing (oxygenic) phototrophs that have been studied to date. No variation of the inorganic core $Mn_4Ca_1O_xCl_{1-2}(HCO_3)_y$ has been identified among them. The PsbA gene encoding the D1 reaction center protein subunit that binds this inorganic core is highly conserved in more than 180 sequences. This invariance of both the protein and cofactors is an extraordinary feature that is not found anywhere else in biology. It is as if nature has performed combinatorial synthesis through evolution over 2.2–3.8 billion years, using all possible ecological habitats that are permissive of photosynthetic metabolism and has been able to invent *only one biological blueprint for water splitting.* This lesson is vital to appreciate by all who are engaged in creating biomimetic catalysts or engineered PSII enzymes for practical applications.

Two applications for which catalysts are sought are the direct solar splitting of water for hydrogen production, and the reversible reduction of O_2 to water in fuel cell cathodes. Nature uses abundant metals (Mn, Ca) organized into a novel, self-repairing, cluster to achieve water splitting. By contrast, man-made water splitting catalysts use rare noble metals (Pt) that operate inefficiently and create damaging reactive intermediates. The lessons learned from photosynthetic water splitting are beginning to contribute to more practical solutions.

In this article, we offer a brief and select overview of the literature on the atomic and electronic structure of the water-splitting enzyme,[5–7] the chemical basis of its catalysis, and insights learned from functional model complexes. Citations cover the main review articles that are available rather than primary works.

2 THE O_2 CLOCK REACTION STEPS: THE 'S-STATE CYCLE'

The PSII-WOC accomplishes a complex task of converting the one-electron photoexcited state of chlorophyll into the concerted four-electron (all-or-nothing) oxidation of two water molecules. The working model used to discuss the intermediate oxidation states of all PSII-WOC enzymes comes from studies of flash O_2 yield measurements by Joliot and coworkers and the interpretation by Kok and coworkers.[8,9] Illumination of dark-adapted chloroplasts or algal cells with saturating flashes of light leads to the production of O_2 in a characteristic pattern peaking on flash #3 and repeating each four flashes. It was therefore concluded that O_2 production takes place at a catalytic center and that each flash advances the oxidation state of the WOC by removal of one electron. O_2 is formed and released only after four oxidation equivalents are accumulated. The 'S-state cycle' which describes this sequence is shown in Figure 1. The stoichiometry of the inorganic cofactors which make up the WOC is $Mn_4Ca_1O_xCl_{1-2}(HCO_3)_y$ and has been determined by various spectroscopic, extraction, and reconstitution studies.[10–12] The pattern of proton release during the cycle is also known and changes with the pH of the medium and the number of protein subunits present in the PSII complex.[13] Electrostatic effects on ionizable protein residues are involved (Bohr protons) as well as the intrinsic protons released from substrate water molecules. The latter stoichiometry has been estimated to be 1:0:1:2.[14] One or more essential Cl^- ions bind within the PSII-WOC complex and are postulated to play a role in proton transfer from the Mn cluster to the medium.[15] Additional information about the kinetics of the S-state advances, stoichiometry of proton release, and the rate of substrate (water) exchange with bulk water is given in Table 1.

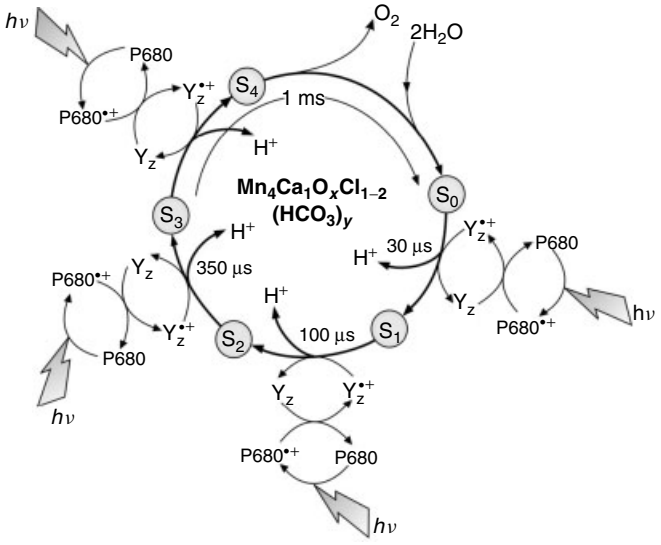

Figure 1 The intermediate oxidation states (S-states) of the PSII-WOC created by single turnover flashes. (Reproduced, with permission, from J. Nield, ''Structural Characterisation of Photosystem II'' Ph.D. thesis, University of London, 1997)

Table 1 Half-life ($T_{1/2}$) for the S-state transitions $S_i \rightarrow S_{i+1}$,[16] the stoichiometry of proton release[14] and the rate of exchange of the two substrate water molecules with bulk solvent water[17,18]

Reaction		# H^+ pH	H_2O exchange rate in S_i	
$S_i \rightarrow S_{i+1}$	$T_{1/2}$ (µs)	7.4/6.3	Fast (s^{-1})	Slow (s^{-1})
$S_0 \rightarrow S_1$	30	0.5/1.5	>100	13.6
$S_1 \rightarrow S_2$	100	1.0/1.1	>100	0.02
$S_2 \rightarrow S_3$	250	1.5/0.5	>175	2.0
$S_3 \rightarrow S_4$	1300	1.0/0.9	37.5	2.0

3 X-RAY DIFFRACTION (XRD) STRUCTURE OF THE PSII PROTEIN COMPLEX

Three XRD models of the PSII-WOC complex from a thermophilic cyanobacterium *Thermosynechococcus* species have been published at resolutions ranging from 3.8 to 3.5 Å.[19–21] The most complete data set was calculated by the method of multiple isomorphus replacement using six heavy atom derivatives and has substantially reduced residuals (R-factor = 30.4% at 3.5 Å resolution vs >53% for the other structures). Hence, we shall discuss this more refined model.[21] The crystallographic asymmetric unit contains a dimer of PSII (640 kDa mass; dimensions: 105 Å depth, 205 Å length, and 110 Å width) with two nearly identical monomers. Within the PSII dimer, monomers are related by noncrystallographic twofold axis perpendicular to the membrane plane. Each monomer consists of 16 integral membrane subunits composed of 35 transmembrane helices and 3 peripheral subunits. The monomer is characterized by pseudo 2-fold symmetry, which rotates the D1, CP47 and *PsbI* subunits into the D2, CP43 and *PsbX* subunits. Each monomer contains 36 chlorophyll *a* (Chl), 7–8 all-trans β-carotene molecules, 1 WOC (Mn_4Ca cluster), 1 heme *b*, one heme *c*, 2 plastoquinones, 2 pheophytins, 1 nonheme Fe, and 2 putative bicarbonate molecules. A stoichiometry of 4Mn and 1 Ca for the WOC was previously established from several lines of evidence, including ^{55}Mn hyperfine structure in EPR,[22]

Mn EXAFS and the rate of O_2 evolution activity during light-driven reconstitution of the free inorganic cofactors to apo-WOC-PSII complexes (photoactivation).[12]

3.1 Charge Separation

Light-driven electron-transfer steps among pigments within the reaction center (RC), composed of the D1 and D2 subunits, serve to trap the light energy delivered from the inner antennas (CP43 and CP47) or outer antennas complexes. Figure 2 depicts the cofactors involved in these electron-transfer reactions. Upon illumination, an electron is transferred *ca.* 35 Å across the membrane from the excited primary electron donor P680 – comprising one or more of the four Chls symmetrically positioned with the D1D2 RC subunits near the lumenal surface – to the final electron acceptor plastoquinone Q_B via Chl_{D1}, pheophytin ($Pheo_{D1}$), plastoquinone Q_A, and nonheme Fe(II). After accepting two electrons and undergoing protonation, plastoquinonol $QH_{2(B)}$ is released from PSII into the membrane matrix. The photo-generated cationic radical $P680^{\bullet+}$ is reduced by a tyrosine residue known as Tyr_Z (D1Tyr161) to generate a neutral tyrosine radical $Tyr_Z^{\bullet}$ which acts as an oxidant for the water oxidation process at the WOC.

The radical cation $P680^{\bullet+}$ oxidizing potential, recently estimated to be 1.3–1.4 V, exceeds that required for water splitting and is the highest of all types of reaction centers.[23] The two Chls denoted P_{D1} and P_{D2}, equivalent to the 'special pair' of bacteriochlorophylls (Bchl) in the anoxygenic bacterial reaction center (BRC), are rotated by 20° to the membrane normal and separated slightly further (Mg–Mg distance of 8.2 Å) than in BRC. The tetrapyrrole head groups of P_{D1} and P_{D2} are in van der Waals contact, but do not have appreciable π overlap, which could explain why P680 shows more monomeric character and weaker electronic coupling than its bacterial counterpart. P_{D1} and P_{D2} Chls are close to Chl_{D1} and Chl_{D2}, suggesting that the P680 excited state is delocalized over the four Chls and that Chl_{D1}, which is closest to the active branch $Pheo_{D1}$, participates in the primary charge separation. The electrons are transferred from $Pheo_{D1}$ to Q_A, which is a firmly bound plastoquinone. Even though PSII and BRCs utilize different primary quinone acceptors, the Q_A binding pockets are structurally similar.

3.2 The Water-splitting Center[21]

The Mn_4Ca cluster is asymmetrically located off the pseudo twofold symmetry axis that relates the 4 Chl molecules comprising P680 and approximately 8 Å below the mean interface of the transmembrane domain. The edge of the closest Chl of P680 is located 8.1 Å from the edge of the photooxidizable tyrosyl radical Tyr_Z (closest non-H atoms) and the latter is located 5.1 Å to the Ca atom and 6.5 Å to the closest Mn atom. This asymmetrical location likely contributes to the strong bias for charge separation involving the closest branch of RC Chls. Water molecules are presumed to fill the gap between the Mn and Tyr_Z. The phenoxyl hydrogen of Tyr_Z is hydrogen bonded to D1His190 and is the presumed proton acceptor required for stable photooxidation to form the neutral

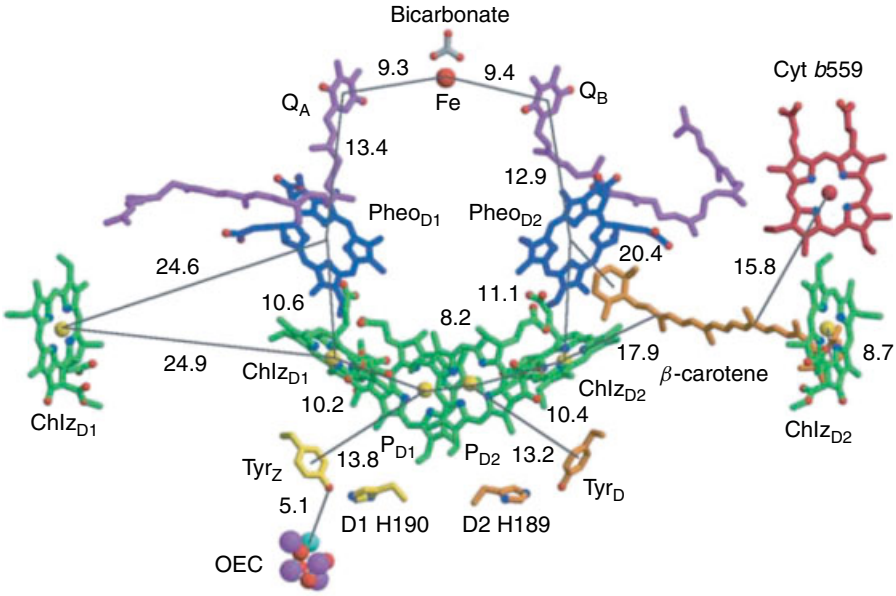

Figure 2 XRD model of the cofactors bound to photosystem II RC core and the water-oxidizing complex. The view is perpendicular to the membrane normal. (Reprinted with permission from K. Ferreira, T. Iverson, K. Maghlaoui, J. Barber and S. Iwata, Science Express, DOI 1093087 (2004). © 2004 AAAS)

tyrosyl radical. Together with the D1Glu189 these residues form hydrogen bonds that have been proposed to be involved in proton ejection into the lumenal space.[24] The distances and geometry provide no support for a mechanism in which Tyr_Z directly abstracts a H atom from substrate water bound to the Mn cluster. However, proton-coupled electron-transfer steps involving other bases in the active site may be involved as proton acceptors.

All of the protein ligands to the Mn_4Ca cluster come from side chains from three different domains of the D1 subunit and one domain of CP43. In D1 these domains are the carboxyl terminus (between H332 and D342), two residues within the interhelical CD luminal loop (D170 and E189), and one residue in the interhelical AB loop (D61). No homology to other protein folding domains is evident.

4 ATOMIC STRUCTURE OF THE INORGANIC CORE FROM XRD AND SPECTROSCOPY

The electron density attributed to the Mn_4Ca cluster is described as 'capped tetrahedral' when contoured at 8σ, with 4 metal atoms in the large end and one in a connected small end (Figure 3). A series of difference Fourier omit maps accommodates a tetrahedral array of 4 metal ions (3Mn + Ca) in the large end and one Mn in the small end. The small protruding density has been assigned to 1Mn based on comparing the anomalous scattering of X rays that are preferentially absorbed by Mn. A Ca atom is located in one of the corners of the tetrahedron based upon anomalous diffraction data taken at the Ca absorption edge. The presence of Ca is supported also by compelling evidence from three types of EXAFS measurements obtained at the Mn-, Ca- and Sr edges.[25] The EXAFS data clearly show that Ca is located at ~3.4 Å to Mn, but had anticipated only 1 or 2Mn scatters at this distance, not 4Mn as proposed in the XRD model. The intermetal distances within the cube are not adequately resolved in the XRD data and have been set equal for simplicity, yielding a symmetrical trigonal prism of $CaMn_3$. The authors postulate four bridging oxides (not directly observable) linking the tetrahedral array of $CaMn_3$ atoms, with one of these oxides (μ_4-oxo) bridging to the fourth Mn atom external to the cube (Figures 3 and 4). The resulting $CaMn_4O_4$ cluster can be classified also in terms of the two types of oxide bridges $(\mu_3\text{-oxo})_3(\mu_4\text{-oxo})$ that make up the core. The resulting $CaMn_4O_4$ core is novel; no exact structural analogs have been synthesized, although all manganese-oxo cubanes containing the $[Mn_4O_4]^{n+}$ are known.[26] Mn EXAFS and ^{55}Mn magnetic hyperfine (EPR) data had previously established the Mn stoichiometry of the WOC and were compatible with 8 possible Mn_4O_x core geometries, one of which has the same topology as the XRD model.[22,25] However, both the EXAFS and EPR data require that a lower symmetry cluster must exist in S_1 and S_2, with Mn EXAFS-derived intermanganese distances of 2.7 Å and 3.3 Å in S_1. This asymmetry could be accommodated if some of the bridging oxygen atoms are water or hydroxide molecules.

The 3Mn atoms within the cubane core each have one terminal carboxylate ligand, two from D1 (D342, E189) and one from CP43 (E354), while one Mn has an additional histidine ligand from D1 (H332). A proposed μ-oxo bridge that lies at the corner of the cube trans to Ca is H-bonded to a histidine of D1 (H337). The Mn atom external to the cube is ligated to two carboxylates from D1 (D170 and E333), two proposed water molecules (one of which is H-bonded to aspartate-61 carboxylate from D1), and an unidentified

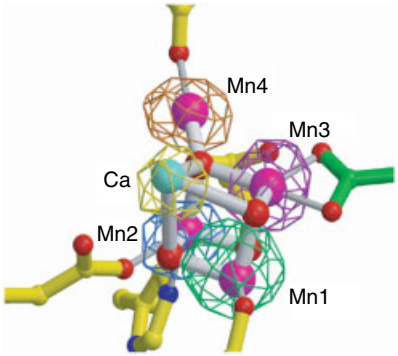

Figure 3 The electron density map of the Mn_4Ca cluster, calculated after omission of each metal of the WOC. The maps are contoured at 8σ for Mn1, Mn2, and Mn3 and 7σ for Mn4 and Ca. (Reprinted with permission from K. Ferreira, T. Iverson, K. Maghlaoui, J. Barber and S. Iwata, Science Express, DOI 1093087 (2004). © 2004 AAAS)

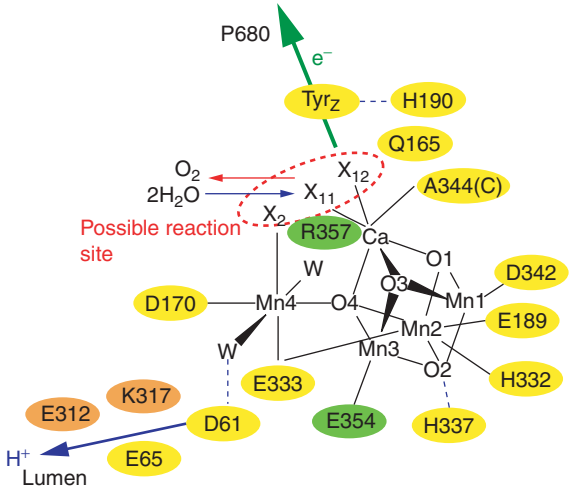

Figure 4 Schematic coordination of the WOC, its protein ligands and other important residues. Residues in D1, D2, and CP43 subunits are shown in yellow, orange, and green, while X_{11}, X_{12}, and X_2 denote nonprotein ligands, possibly substrate water binding positions or bicarbonate site. (Reprinted with permission from K. Ferreira, T. Iverson, K. Maghlaoui, J. Barber and S. Iwata, Science Express, DOI 1093087 (2004). © 2004 AAAS)

heavier scatterer X1 (possibly Cl^-, SO_4^{2-} or CO_3^{2-}). The Ca atom has no protein ligands but is coordinated to two solute molecules X21 and X22 having electron density greater than water (postulated as Cl^-, SO_4^{2}, or CO_3^{2-}). Arginine residue Arg357 from CP43 is positioned with its side chain fully extended and its cationic guanidinium group interacting with the nonprotein ligand X1 with a $N\cdots X_1$ bond length of 1.9 Å. In the current model the authors have positioned a tridentate carbonate ligand bridging between the exo-cuboidal Mn and Ca at these positions (both X22 and X23 carbonate(O)$\cdots$Ca distances = 2.26 Å). The authors postulate that these sites constitute the likely substrate water sites.

The net charge of the core of the WOC is not known experimentally. The XRD model for the $[Mn_4CaO_4]^n$ core suggests charges of $n = 6+$ or $8+$ for S_1 (assuming $4Mn^{III}$ or $2Mn^{III} + 2Mn^{IV}$ as suggested by EPR and Mn XAS, respectively). Assuming that the coordinated protein carboxylates are ionized, there are a total of 6− charges from the ligands. This leaves a minimal net charge for the WOC of zero or 2+, respectively, and possibly greater assuming that some of the oxo bridges are protonated. Charge neutralization within buried active sites suggests that the nonprotein ligands (X1, X22, X23 and possibly other Mn coordinate sites) are most likely anionic ligands. The possibilities include solute (OH^-), other native cofactors required for water splitting (Cl^-, CO_3^{2-}) or precipitant (SO_4^{2-}).

5 INSIGHTS FROM MUTAGENESIS

The XRD model of the PSII monomer contains assignments for 19 of the 21 known PSII gene products except for the genes PsbW and PsbY. Mutagenesis studies have been carried out on some of these protein subunits, with the majority directed at the D1 protein and more recently CP43.[24,27–29] The consequences of point mutations in selected residues of the D1 and CP43 proteins are summarized in Figure 5 and discussed below.

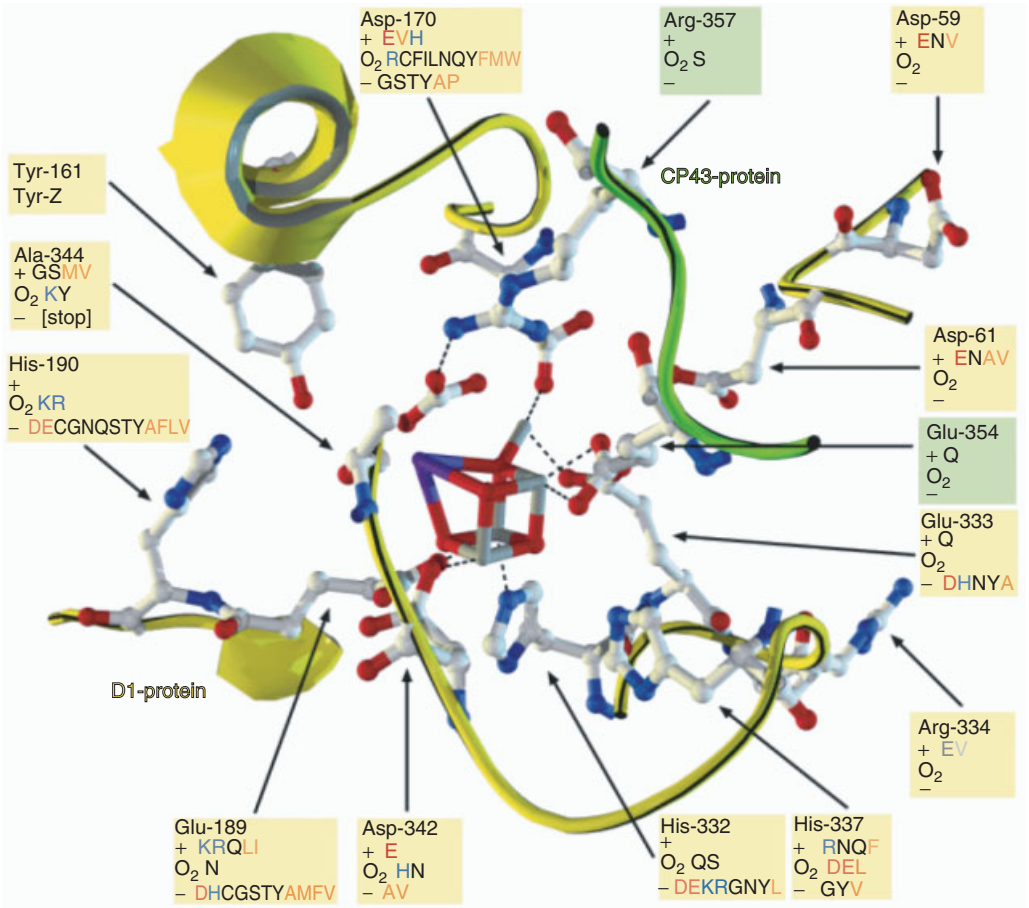

Figure 5 Consequences of point mutations in D1 (yellow) and CP43 (green). In the boxes, the first line (+) indicates amino acids mutations that support photoautotrophic growth (light + CO_2) and evolve O_2. The second line (O_2) indicates mutants that do not grow photoautotrophically but retain an initial O_2 evolution rate when grown heterotrophically (≥5% vs. the wild-type strain). The third line (−) indicates lethal mutants that do not grow photoautotrophically, have no O_2 evolution activity, and in some cases no photooxidizable Mn. Amino acid color coding: acidic (red), basic (blue), hydrophobic (brown)

The primary aims of mutagenesis are to identify those amino acid residues that control the assembly and functioning of the $Mn_4Ca_1O_x$ cluster and the reactivity of D1Tyr$_Z$161.

Mutagenesis studies have identified three domains of the D1 protein implicated in assembly of a stable WOC or expression of O_2 evolution activity. In D1 these domains are the carboxyl terminus, the interhelical CD lumenal loop, and residues in the interhelical AB lumenal loop. These loci agree with the amino acid sites identified by XRD.

Within the carboxyl-terminus of D1, multiple residues play a role in stabilizing the WOC by interaction with one or more of the three internal Mn ions of the $Mn_3Ca_1O_x$-cube. Studies have been performed on D1Ala244, D1Asp342, D1His332, D1His337, D1Arg334, and D1Glu333, of which Asp342, His332, and Glu333 ligate the $Mn_4Ca_1O_x$-cluster according to the crystal structure (see Figure 5). There is solid evidence from pulsed EPR studies and FTIR for one histidine ligand to the $Mn_4Ca_1O_x$ cluster which may correspond to D1His332. Most mutants of the ligating amino acid residues do not grow photoautotrophically and possess diminished oxygen evolution rates. Although the Ala344 is not ligating manganese (Reanalysis of the 3.6 A XRD data[30] has shown that two oxos at the corners of the Mn_3CaO_4 cubane-like core (O_1 and O_3, Figure 4) interact by hydrogen bonding to carboxylate residues (D1-Glu189 and D1-Ala 344-C-terminus). These oxos exhibit bonding interactions consistent with identification as water molecules. Mutagenesis studies are consistent with these carboxylate residues serving in proton pathways for substrate water deprotonation. On this basis and other evidence, the O_1 and O_3 corner sites have been proposed as the substrate water oxidation sites[30]), there is a requirement for the presence of an amino acid residue at this position.

The interhelical CD lumenal loop contains the Tyr$_Z$ (D1Tyr161), probably hydrogen bonded to D1His190. It contains the D1Asp170 residue which ligates the high affinity Mn (exocubical Mn). Mutagenesis on this important residue shows that Glu, His, and even Val mutants grow photoautotrophically, while 11 other mutants show at least some oxygen evolution, albeit only when grown heterotrophically on glucose. The latter mutants fail to grow photoautotrophically apparently due to photoinactivation of the WOC. It was concluded from EPR measurements that Asp170 ligates the high affinity Mn site, as the binding and/or photooxidation of Mn(II) was altered in mutants at that site. Remarkably, some positively charged, polar, and hydrophobic mutants of D1Glu189, which is a ligand of the $Mn_4Ca_1O_x$ cluster, show photoautotrophic growth. An hypothesis is that mutants at this residue are involved in a network of hydrogen bonds, possibly in which additional bicarbonate or chloride ions might compensate for loss of the carboxylate charge in some mutants.

According to mutagenesis studies, the amino acid residues in the interhelical AB lumenal loop are involved in coordination of the Ca^{2+}, especially D1Asp59 and D1Asp61. The crystal structure does not yield evidence for direct binding of these residues to Ca. All examined mutants at these positions exhibit an elevated requirement for Ca^{2+} and show photoautotrophic growth. The mutagenesis and XRD results appear inconsistent but may not be. Since the Ca^{2+} binding assays used with the mutants are actually O_2 evolution assays performed in the presence of Mn, these assays reflect the cooperative binding between the high affinity Mn and Ca sites during assembly.[12]

Mutagenesis studies have examined the CP43 protein. First segment deletion studies were conducted, followed by site-directed mutagenesis. The point mutant, Glu354Gln, exhibits reduced photoautotrophic growth rate, although normal PSII content (e.g. no photoinactivation) and an 80% reduction in the O_2 evolution rate due to a specific impairment to the WOC.[31] The Arg357Ser mutant is the only available mutant at this site. It is unable to grow photoautotrophically, but does grow heterotrophically on glucose. It accumulates a normal amount of PSII core proteins, but these exhibit low electron-transfer rates, weak O_2 evolution activity (10%) and strong photoinactivation kinetics (fourfold).[32] These results clearly show an important role that both of these residues play in water-splitting chemistry, as would be expected by the XRD structure (Figure 4).

Mutagenesis studies together with the emerging PSII XRD structures at higher resolution offer future opportunities for detailed mechanistic insight at the molecular level in the coming years.

6 Mn OXIDATION STATES AND ELECTRONIC (SPIN) STATES

The electronic states of the $Mn_4Ca_1O_x$ cluster, for example, the spatial distributions and energies of the electrons in the various S-states are vital to understanding water-splitting chemistry. Tools such as electron paramagnetic resonance (EPR) and X-ray absorption spectroscopies (XAS) have been indispensable to characterize both the redox chemistry of PSII-WOCs and the atomic structure of the inorganic core. Historically, EPR provided the first experiments to identify an electronically coupled Mn cluster at the catalytic site. Shortly thereafter, spectral simulations of the extensive ^{55}Mn hyperfine structure in the S_2 oxidation state indicated electronic coupling of 4Mn ions (Mn^{3+} and Mn^{4+} oxidation states) in a low-spin ground state ($S = 1/2$). EPR signals are now available for four of the five S-states and each in multiple perturbed forms.[22,33–36] An important conclusion is that all of the S-states are formed in low-spin ground electronic states in native (unperturbed) PSII-WOC complexes (Table 2).[22] This conclusion comes from measurements of the electronic Zeeman g−factor and zero-field splittings (for $S > 1/2$). The ^{55}Mn hyperfine structure (magnetic and quadrupole tensors) has given a detailed description of how the unpaired spin density is distributed among the four Mn ions in the S_2 state.

Table 2 Electronic spin states (Zeeman g factors): S ($g_{\text{effective}}$) and changes in the room temperature magnetic susceptibility ($\Delta\chi$) upon advances in oxidation states of the spinach WOC induced by single turnover flashes in PSII complexes. *Syn.* denotes *Synechocystis* 6803[a]

	S_0	S_1	S_2	S_3
S (g_{eff}) ground first excited	1/2 ($g = 2$)	0 ≥ 1 integer ($g = 4.8$ spinach $g = 12$ *syn*)	1/2 ($g = 2$) 5/2 ($g = 4.1$)[a] 7/2 ($g = 10, 6$)[a]	0 ≥ 1 integer ($g = 12, 8, 6.7$)
$S_i \rightarrow S_{i+1}\Delta\chi$ (μ_B^2)	~0	+ (14–17)	~0	+10 (8 from O_2)

[a]The S = 5/2 and 7/2 spin states become ground states in modified samples.

The resulting spin densities are compatible with a limited set of cluster geometries and Mn oxidation states.

The lowest spin configuration occurs when all 4 paramagnetic Mn ions are coupled by pairwise antiferromagnetic interactions via bridging ligands, corresponding to favorable bonding interactions between the Mn electrons. In addition, low-lying excited electronic states are found to be thermally populated, as revealed by both EPR and magnetic susceptibility measurements in all S-states.

Additionally, the S_2 state (and probably others) can be produced in different ground states having discrete spin values S = 1/2, 5/2 or 7/2, depending upon how it is prepared from the S_1 state. For example, lower temperature illumination favors the S = 5/2 state, while NH_3 inhibition involves binding to a site between Mn ions that forms a different S = 1/2 state characterized by a redistribution of spin densities. Near-IR illumination of Mn^{3+} electronic transition forms an excited state that relaxes to a new ground state either an S = 5/2 or 7/2 state. These conditions change the ordering in energy of these discrete electronic spin states by changing the relative strength or number of intermanganese couplings and by changing the Mn d^n electronic configuration. The former is mediated by the bridging ligands while the latter is determined by the ligand field strength and symmetry. This flexibility of the electronic states does not happen in binuclear clusters or in higher nuclearity clusters that possess only nearest neighbor spins (e.g. linear). Hence, the Mn ions in the Mn_4O_x core are arranged with bridges between more than one other Mn ion. These competing pathways orient the Mn spins such that both low- and intermediate-spin configurations can be produced by modest changes to the intermanganese couplings. This phenomenon is called spin frustration. There are only 8 possible Mn_4O_x geometries which can account for the multiple spin configurations observed for the S_0 through S_3 oxidation states. Three of these cores are depicted in Figure 6. Topologically, they may be called funnel (4), cubane (12), and open cubane (13).

Among these $8Mn_4O_x$ core types, only those that produce the same distribution of unpaired electron spin density need to be considered further as structural models of the WOC. This distribution can be obtained from the ^{55}Mn hyperfine structure observable in EPR and ENDOR measurements of the S_0, S_1, and S_2 states.[22,34] A simple ionic model to predict the Mn spin densities has worked well in simulating the ^{55}Mn hyperfine structure, but not all 8 possible topologies have been fully investigated yet. The S_1 state EPR signal exhibits ^{55}Mn hyperfine structure with 21 lines separated by one observable hyperfine constant and a binomial pattern of intensities consistent with 4 magnetically equivalent ^{55}Mn ions (I = 5/2).[34] This indicates an approximately uniform spin density on all 4Mn ions and thus a single Mn oxidation state is indicated.

The native S_2 state EPR signal (ground spin S = 1/2) illustrates a more asymmetric distribution of spin densities. Assuming the Mn oxidation states are Mn_4(3III,IV) the deduced spin densities that simulate the EPR spectrum are given in Figure 7 (ionic model). This is illustrated using a $Mn_4O_2(OH)_2$ cubane-type model, although other spin-frustrated topologies like the open cubane core (13) in Figure 6 are also suitable. Future EPR simulations should examine the open cubane core (13) and the influence of Ca^{2+} on

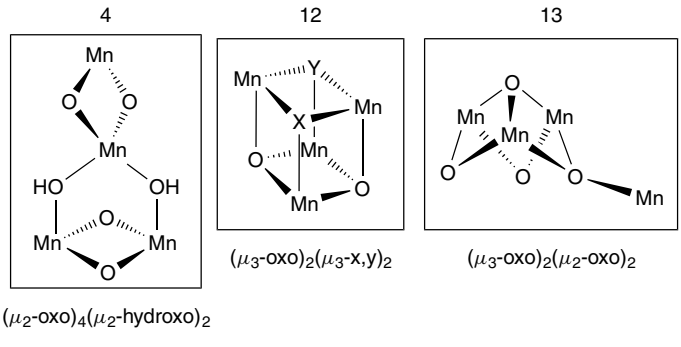

Figure 6 Three of the eight possible Mn_4O_x core topologies that could give rise to the observed spin states[22]

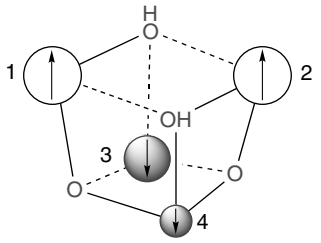

Figure 7 Unpaired spin density distribution on the four Mn ions in the native S_2 state (total spin S = 1/2). The size of the spheres reflect the spin densities: 5/3, 5/3, −4/3, −1. The two shades of sphere indicates + and − spin density. A distorted $Mn_4O_2(OH)_2$ cubane core was postulated

spin densities. A higher oxidation state Mn_4(III,3IV) has been proposed for the S_2 state based upon XAS and some EPR experiments, so that the question of Mn oxidation states remains unresolved. A good summary of the debated interpretations can be found in the following articles.[22,34]

Changes in the room temperature magnetic susceptibility upon photooxidation between S-states (Table 2) reveals that the third photooxidation step, for example, $S_3 \rightarrow S_0$, yields a large increase equal to 10 squared Bohr magnetons ($\mu_\beta{}^2$), comprising $8\mu_\beta{}^2$ owing to the O_2 product (proved by use of glucose oxidase trap) and $2\mu_\beta{}^2$ from reduction of the Mn_4 cluster. The O_2 product is therefore formed in the S = 1 (ground) triplet spin configuration ($\mu_{\text{eff}}{}^2 = 4S(S+1)$ for spin-only magnetism), as was anticipated based on thermodynamic predictions. The second and fourth photooxidation steps produce small or no change in $\Delta\chi$, while the first photooxidation step which converts the resting S_1 state to S_2 has a very large increase equal to $14-17\mu_\beta{}^2$. This large increase for S_1(resting) $\rightarrow S_2$ is not cyclic on the second turnover of S_1 and reflects the larger $\Delta\chi$ increase seen when the S_1 state is dark adapted for 15 minutes or longer prior to illumination. Hence, the active S_1 conformation which cycles during continuous O_2 production possesses considerably weaker antiferromagnetic couplings between some of the Mn spins. Studies of Mn_xO_y clusters reveals that ferromagnetic intermanganese pairings are not found between Mn ions in mono- and di-μ_2-oxo bridged Mn^{2+}, Mn^{3+} and Mn^{4+} complexes (dimers), but are observed in μ_3-oxo and μ_4-oxo bridged clusters where three or four Mn ions compete for spin alignment, respectively. These additional couplings produce spin frustration within the trinuclear and tetranuclear Mn-clusters causing a greater density of low-lying electronic spin states and an increase in χ. The very large increase in χ on the S_1(resting) $\rightarrow S_2$ step reflects conversion of a less frustrated, relaxed, $Mn_4Ca_1O_x$ topology to a more frustrated spin topology (exhibiting an increase in the number of Mn-μ-oxo bonds or a more equitable distribution of exchange couplings between the existing Mn-μ-oxo bonds.). Model compounds have shown that a plausible chemical process that could produce such a large increase in χ is the formation a μ_3-hydroxo/oxo bridge between three Mn ions, as occurs upon deprotonation of an aquo/hydroxo ligand.

7 ENERGETICS OF S-STATE TRANSITIONS: FREE ENERGY AND ACTIVATION ENERGY BARRIERS

The kinetics and thermodynamics of individual steps in the catalytic S-state cycle have been measured by time-resolved UV-absorption changes of Mn and lead to the picture shown in Figure 8 and Table 1.[13,37] The half-lives for reduction of the Tyr_Z radical ($Y_z^\bullet$) by the Mn cluster after flash excitation in the first three steps ($S_iY_z^\bullet \rightarrow S_{i+1}Y_z$; $i = 0,1,2$) are in the range of 30–50 μs, whereas the last step ($S_3Y_z^\bullet \rightarrow S_0Y_z + O_2$) is rate-limiting with a half-life for S_3 of 1 ms (Table 1). The H/D kinetic isotope effects using D_2O as substrate have been measured by three different groups and fall in the range for all four steps $k_H/k_D = 1.3-1.4$, 1.3–2.9, and 1.5–2.3.[38,39] The UV and near-IR spectral changes during S-state cycling have been attributed to oxidation of high-spin Mn(III) ions.[35]

The thermodynamic driving force (ΔG) for each of the S-state transitions has been estimated from measurements of the temperature-dependent equilibrium constants for the light-induced transient intermediate states: $P680^+/Y_z$ and $Y_z^\bullet$/WOC(Mn).[39] These values were then placed on

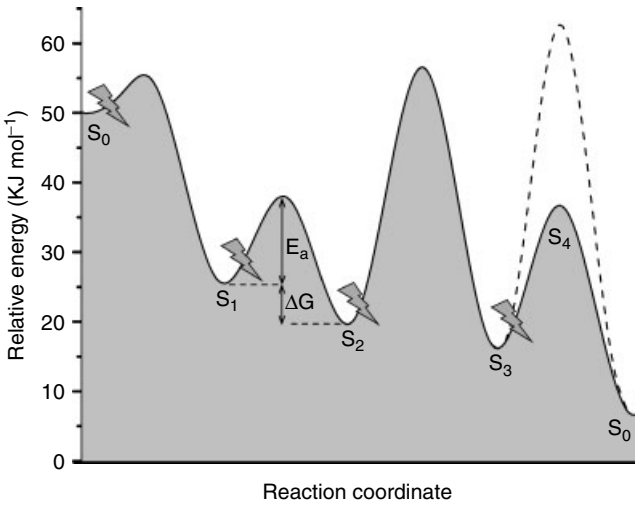

Figure 8 The free-energy changes of the S-state intermediates and their transition states: the reactions $S_iY_z^\bullet \rightarrow S_{i+1}Y_z (i = 0-2)$ and $S_3Y_z^\bullet \rightarrow S_0Y_z + O_2$ for spinach PSII membrane fragments measured at room temperature. The dashed line indicates a higher energy transition state that exists for $S_3Y_z^\bullet \rightarrow S_0Y_z + O_2$ when measured at T < 279 K. E_a = Arrhenius activation energy; ΔG = calculated net free energy change on each turnover. The constant energy offset for the cycle ($\Delta G = 42.9\,\text{kJ mol}^{-1}$) reflects the combined effects of oxidation $Y_z \rightarrow Y_z^\bullet$ and conversion of dark-adapted (resting) S_0 to active S_0-states

an absolute free energy scale using an estimated value for the $P680^+/P680$ reduction potential. The free energies vary between approximately $-4\,kJ\,mol^{-1}$ and $-24\,kJ\,mol^{-1}$ (Figure 8). Also shown are the corresponding experimental activation energies which vary between $+5\,kJ\,mol^{-1}$ and $+36\,kJ\,mol^{-1}$.[39] The highest activation barrier is found for the S_2 to S_3 step and was interpreted (together with EXAFS data) as evidence for a structural rearrangement of the Mn cluster which increases the intermanganese distances in two Mn_2 pairs by 0.1–0.15 Å.

8 SUBSTRATE BINDING, EXCHANGE, AND MECHANISM OF O_2 EVOLUTION

$^1H/^2H$-ENDOR and ESEEM methods have provided good evidence for water molecules in the active site.[40–42] Two exchangeable protons located at 2.5 Å have been assigned to a water molecule directly bound to a Mn ion in the native S_2 state.[42] A second pair of exchangeable protons lacking scalar hyperfine coupling but with large dipolar coupling is located at 2.7 Å from the nearest spin density center (Mn).[42] The latter water site is unlikely to be on Mn and has been suggested to represent water bound to the Ca^{2+} site. Both sites are located in an aqueous-like environment with additional exchangeable protons attributed to water molecules in the next coordination shell. The assignment of these water ligands as substrate molecules although plausible is speculative.

An alternative approach to characterize the chemical environment of the substrate water molecules is by the rate at which they exchange with bulk water. This experiment has been conducted using rapid-mixing mass spectrometry to measure the isotopic composition of the O_2 product following injection of ^{18}O-water in each S state.[17] Table 1 gives the rate constants for the two exponential kinetic phases that are present in the data. These phases have been attributed to two substrates sites that exchange with bulk water at slow and fast rates. The first conclusion is that there is no evidence for nonexchangeable substrate sites; for example, no irreversible step occurs that is not in equilibrium with bulk water. The authors interpret the rate data as evidence that the slow substrate water is bound to a Mn(III) site in all S-states, while the fast exchange site is unlikely to involve coordination to Mn prior to the S_3 state.

The large (100-fold) decrease in the exchange rate at the slow substrate site in the S_1 state and recovery in S_2 has not been satisfactorily explained, but should prove important in sorting out the correct mechanism. One hypothesis is that the slow exchanging substrate site may help to protect PSII against disassembly of the inorganic core caused by reduction of the S_1 core by diffusible reductants that are present in the cell or chloroplast (H_2O_2, ascorbate, glutathione). Mano *et al*. showed that the reaction of PSII membranes in the S_1 state with H_2O_2 is 100x slower than either the S_2 or S_0 states (catalase activity of PSII) suggesting that the H_2O_2 binding site (catalase dismutation) and the slow substrate site are the same site or are in rapid equilibrium.[12] Both of these sites were found to be distinct from the functional chloride site.

The most recent mass spectrometry data using Sr to replace Ca suggests that the fast exchanging substrate site may involve interaction with Ca.[18] This interpretation agrees with $^1H/^2H$-ENDOR and ESEEM results showing that two water molecules are bound, one to a Mn site and the other to a nonmagnetic site postulated to be Ca.[42]

There has been wide debate about whether the kinetic data for S-state transitions discussed in Section 6 are evidence for concerted H atom transfer or proton-coupled electron transfer (pcet) involving more weakly coupled sites for the proton and electron. The small H/D kinetic isotope effect (KIE) for the S-state transitions (as little as 1.3–1.4) indicates little displacement of the H atom coordinates in the transition state. The 6.5 Å distance between the phenol oxygen of Tyr_Z and the nearest Mn ion observed in the XRD structure of PSII-WOC essentially eliminates a direct concerted H atom transfer mechanism, as the distance is too far for tunneling of H atoms. This has led to two pcet models for the S-state transitions that enable the longer-range, delocalized, electron-transfer pathway to be thermodynamically coupled to the shorter range proton transfer pathway of the reaction.[14,24,28] The first model involves oxidation of the $Mn_4Ca_1O_x$ cluster (molecular orbitals localized thereon) that is coupled to the ionization of substrate protons. The Tyr_Z radical is both the electron and proton acceptor in one view (phenol oxygen proton site). Another view argues that these functions are separated, such that the proton is delivered to other auxiliary proton carriers (water, bicarbonate, amino acids (Reanalysis of the 3.6 A XRD data[30] has shown that two oxos at the corners of the Mn_3CaO_4 cubane-like core (O_1 and O_3, Figure 4) interact by hydrogen bonding to carboxylate residues (D1-Glu189 and D1-Ala 344-C-terminus). These oxos exhibit bonding interactions consistent with identification as water molecules. Mutagenesis studies are consistent with these carboxylate residues serving in proton pathways for substrate water deprotonation. On this basis and other evidence, the O_1 and O_3 corner sites have been proposed as the substrate water oxidation sites[30])) in a distributed hydrogen-bonded network eventually reaching the aqueous lumen. In both cases, the reduction of the Tyr_Z radical is coupled to its protonation, either by a substrate proton or an alternative proton donor, likely D1His190.

No direct evidence for Mn(V) or peroxide-like intermediates have been observed yet in any native S_i state. However, release of hydrogen peroxide occurs in a modified S_2 state formed under a variety of conditions (removal of Cl^-, replacement of Cl^- by F^- and solubilization with lauryl choline chloride)(reviewed in[12]). These results show that the driving force for HO–OH bond formation already exists at the modified S_2 oxidation level.

There is little experimental information about the O–O bond formation step in the native S_4 state. Two general

mechanisms for the O–O bond formation step have been postulated (Figure 9), although definitive evidence to distinguish these possibilities or others is still lacking. The first mechanism (Figure 9(a)), involves homolytic intramolecular bond formation from two bridging substrate oxygen atoms in the $Mn_4Ca_1O_4$ core. In this mechanism the O=O bond enthalpy must contribute to overcoming the favorable Mn–O bond enthalpy in the transition state for reaction to occur. There is definitive experimental proof that this reaction coordinate is thermodynamically possible in symmetrical $Mn_4O_4^{6+}$ cubane clusters because they have long (e.g. weak) Mn–O bonds, but not in simpler $Mn_2O_2^{2+/3+/4+}$ cores which have much shorter (e.g. stronger) Mn–O bonds (see final section).[43]

A heterolytic pathway, Figure 9(b), has been proposed which involves attack by a nucleophilic OH^-, possibly generated by ionization of water bound to Ca^{2+}, at an electrophilic oxygen atom. The latter oxygen atom has been attributed to either a putative Mn(V)=O 'manganyl oxo' intermediate as envisioned in Figure 9(b),[44] or a bridging oxyl radical (μ_2-O$^\bullet$).[45] The latter proposal is supported by electron structure calculations showing that bridging μ_2-oxos can be sufficiently electron deficient in special Mn_xO_y topologies that nucleophillic attack may be possible by OH^-.[45]

Bicarbonate influences the activity of electron donation from Mn^{2+} to apo-WOC-PSII complexes depleted of manganese.[46] Photoactivation data show that bicarbonate interacts with the high affinity Mn^{2+} and stabilizes the photooxidized Mn^{3+} product during assembly of the WOC. These data and the hypothesis from XRD allowing the presence of bicarbonate as a core ligand in the holoenzyme (Figure 4) open up interesting new mechanistic possibilities to consider.

An alternative heterolytic pathway shown in Figure 10(a) can be envisioned based on the XRD evidence suggesting a μ_4-oxo (Figure 4). The μ_4-oxo will be electron-deficient and thus forms a potentially reactive site for O–O bond formation with a nucleophilic oxyanion. Here we postulate that the carbonate ion in the active site attached to Ca, Mn, and Arg357 residue serves as the nucleophile by forming peroxycarbonate, transiently as a bound intermediate that decays to the O_2 product. This proposal is supported by the occurrence of carbonates as nucleophiles in organic hydration reactions and the formation of peroxycarbonate as metastable intermediate in carbonate chemistry.[47] Unlike pathway Figure 9(b), which must form the Mn(V) oxidation state in order to form an electrophilic manganyl oxo complex, pathway Figure 10(a) produces a highly activated μ_4-O at the Mn(IV) level.

An alternative homolytic pathway shown in Figure 10(b) can also be envisioned in which intramolecular O–O bond formation occurs between the electrophillic μ_4-oxo and a transient nucleophilic μ_2-oxo released from Ca upon rearrangement of the carbonate ligand from monodentate to bidentate coordination. The figure shows the anticipated

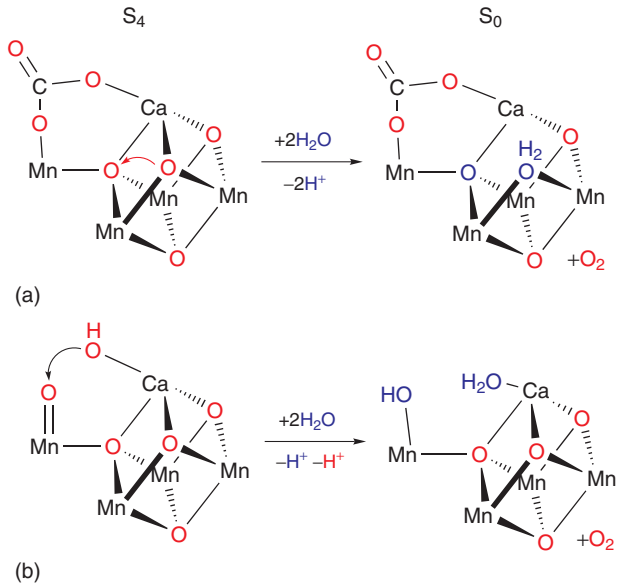

Figure 9 Two general mechanisms postulated for O–O bond formation. (a) involves homolytic intramolecular bond formation from two bridging substrate oxygen atoms, while (b) involves a nucleophilic attack at a an electrophilic oxygen atom

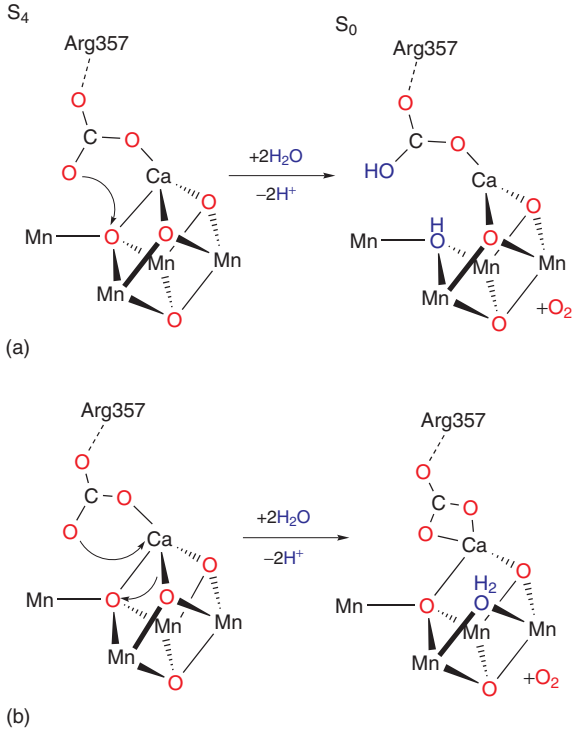

Figure 10 Two alternative hypothesized mechanisms for formation and release of oxygen in the $S_4 \rightarrow S_0$ step, incorporating hints yielded by the emerging crystal structures at higher resolution. (a) shows a heterolytic mechanism in which the electron-deficient μ_4-oxo acts as an electrophile, while (b) shows a mechanism involving the Ca^{2+} ion leading to the formation of a peroxo-intermediate

bond isomerization sequence leading to a transient peroxo-intermediate that decays to the O_2 product. In both of the mechanisms depicted in Figure 10(a) and (b), the Ca^{2+} participates directly in the O–O bond formation step. This key feature is in agreement with the experimental data on O_2 release in inorganic mutants replacing Ca^{2+} with Sr^{2+} (Reference 48).

With the rapid advances in knowledge that are taking place in the chemical basis of PSII catalysis, there will surely be exciting times ahead in sorting out these proposals for the mechanism of water oxidation.

9 WHY MANGANESE? INORGANIC MUTANTS

Several factors may have conspired to make manganese the universal metal for catalyzing water splitting in all oxygenic phototrophs. Transition metals are the clear winners versus main group atoms at storing/delivering large units of energy in the form of redox reactions, for example, atom transfer reactions, in contrast to acid-base chemistry and ion concentration gradients. This preference arises because transition metals store and deliver energy in the form of both charge (the number of electrons) and bond strengths (potential and kinetic energy of electrons and nuclei). Their versatility originates from the greater number and smaller energy spacing of their valence d orbitals which facilitates matching with substrate orbitals for maximal bond strength and accommodates a wider range of geometries. A direct consequence is that the geometrical constraints can be relaxed in cases where the redox changes involve nonbonding d orbitals. For the same reasons, the activ ation barriers between redox states in multistep catalysis are usually lower.

Phototrophs take up Mn^{2+} but use it in the WOC in the Mn^{3+} and Mn^{4+} oxidation states. Mn^{2+} is highly soluble, has weak or modest affinity for simple ligands, speciates as the simple aquo cation in water over a wide pH range and is readily transported into cells by a variety of redundant transport systems. Mn^{2+} is chemically stable in neutral solutions. It auto-oxidizes in O_2 saturated solutions only above pH 9.5 where most phototrophs do not function, or at ambient pH only if exceptionally strong chelates are accessible to stabilize the resulting Mn^{3+} (e.g. pyrophosphate^{4-}). Hence, there is usually no need for chaperone proteins in the cell to deliver Mn^{2+} or to protect the cellular matrix from auto-oxidation. Mn chaperones have not been identified (yet) for assembly of the WOC during biogenesis. What a great savings in energy and complexity for the primitive phototroph that first used Mn^{2+} over other more abundant redox metals (Fe^{2+}) in the anaerobic world when oxygenic photosynthesis was invented. The redox potential for oxidizing Mn^{2+} (aq) $\rightarrow$ Mn^{3+} (aq) $E^0 = 1.3\,V$ closely matches the redox potential of Chl-a, unlike the majority of other soluble transition ions. Thus, the biogenesis of Chl-a in phototrophs enabled the photooxidation of Mn^{2+} to occur on the surface of Chl-a proteins. The resulting Mn^{3+} binds more tightly by ca. $10^{12}-10^{15}$ and thus would be long-lived at the protein site. Importantly, loss of the redox energy by charge recombination is greatly slowed owing to the energy released upon dissociation of a proton to form $[Mn^{III}(OH^-)]^{2+}$ ($pK_a = 0$). Energetically downhill direct electron-hole recombination without reprotonation is also greatly slowed owing to the unusually large vibronic distortion that Mn^{3+} typically produces with its ligand environment (e.g. 1 eV barrier for pseudorotation of the Jahn–Teller axes in MnF_6^{3-}). The photooxidation of a second Mn^{2+} is catalyzed by formation of the first $Mn(OH)^{2+}$ photoproduct, as the OH^- can serve as a better ligand than water to template the binding of the next Mn^{2+}. The efficiency of this assembly process increases in the presence of bicarbonate which is a surrogate for hydroxide and can exist in neutral pH solutions at concentrations several orders of magnitude higher than hydroxide.

These properties of aqueous Mn redox chemistry are all utilized during the light-driven biogenesis of the $Mn_4Ca_1O_x$ core from the free inorganic cofactors and apo-WOC-PSII. Measurements of the kinetics of reconstitution of O_2 evolution activity and proton release during this photoactivation process have resolved three kinetic intermediates:[49] first $Mn^{II}(OH^-)$ or $Mn^{II}(HCO_3^-)$ binds to the high affinity Mn site, involving D1Asp170, followed by a slow (rate-limiting) dark step in which a proton is ejected and the affinity of Ca^{2+} increases substantially. This step is hypothesized to involve a conformational change of the D1 protein (carboxyl terminus or AB loop movement). It is followed by cooperative binding of 3 additional Mn^{2+} and photooxidation steps in rapid succession that are not resolved kinetically. This $1 + 3Mn^{2+}$ sequence and positive cooperativity in Ca^{2+} uptake after the first Mn^{2+} photooxidation step fits well with the XRD structural data. Bicarbonate was shown to specifically increase the affinity of Mn^{2+} at the high affinity site by stabilizing the photooxidized Mn^{3+} state. A second higher affinity bicarbonate site was found that stimulates the rate of photoactivation and was attributed to electrostatic attraction of Mn^{2+} caused by ionization of protein residues or ion-pairing between carbonate and arginine.

A nearly constant yield and rate of photoactivation is found over a 200-fold range in concentrations of Mn^{2+} and Ca^{2+}, provided the ratio is kept nearly constant at about 500 Ca/1Mn. If Ca^{2+} is left out of the solution, binding and photooxidation of many more Mn^{2+} occurs to the apo-WOC-PSII protein and no O_2 evolution activity is observable. Ca^{2+} can be replaced by Sr^{2+} and actually accelerates the assembly process by 4-fold,[12] but the O_2 evolution rate is reduced to 40%, apparently due to a slower terminal step $S_3 \rightarrow S_0 + O_2$.[48] It can be concluded that Ca^{2+} is specifically involved in the O–O bond formation step.

No functional replacement for manganese during the photoactivation process has been found to be effective (yet).

Several 3d, 4d, and 5d transition ions were tried, all at fixed pH (6) and fixed concentration without success.[12] It appears that manganese may be truly unique for biological water splitting.

10 FUNCTIONAL MANGANESE COMPLEXES THAT SPLIT WATER

There have been a large number of examples of Mn-oxo complexes that have contributed important insights to understanding the structure and function of the $Mn_4Ca_1O_x$ core.[43,50,51] However, only three systems have been shown to produce O_2 and will be highlighted here.

10.1 The Dimanganese(III,III)porhyrin Complex

The dimanganese(III,III)porphyrin complex (**1**) depicted in Figure 11 was shown to catalyze the anodic oxidation of water at low conversion ($\leq$8 turnovers). The mechanism appears to proceed by formation of a $[Mn(V)=O]_2$ intermediate (**2**) which has recently been isolated by chemical oxidation with *m*-chloroperoxybenzoic acid (Figure 11). Subsequent acidification of (**2**) yields O_2 in a stoichiometric reaction that does not occur with the corresponding mono-manganese(V) porphyrin, nor with the corresponding $[Mn(IV)]_2$ dimer species. Two mechanisms were considered based on H/D-water isotopic labeling studies and the observation that the acidified intermediate also converts Cl^- to OCl^- quantitatively. The postulated active intermediate is $[H_2O–Mn(V)=O]_2$. This species may produce O_2 either by intramolecular coupling of the oxo groups, or by $[H_2O–Mn(V)=O]$ reaction with free water. The latter reaction could not be excluded, as the oxo in (**2**) exchanges with water rapidly. This chemistry suggests that the homolytic coupling of two electrophilic oxos is an observable pathway for O–O bond formation with strong π-acceptor porphyrin ligands. Geometrical constraints on the intermanganese distance and orientation imposed by the covalent bridge linking the porphyrin ligands were found important for O_2 formation in earlier work, further implicating a homolytic intramolecular pathway is observed.

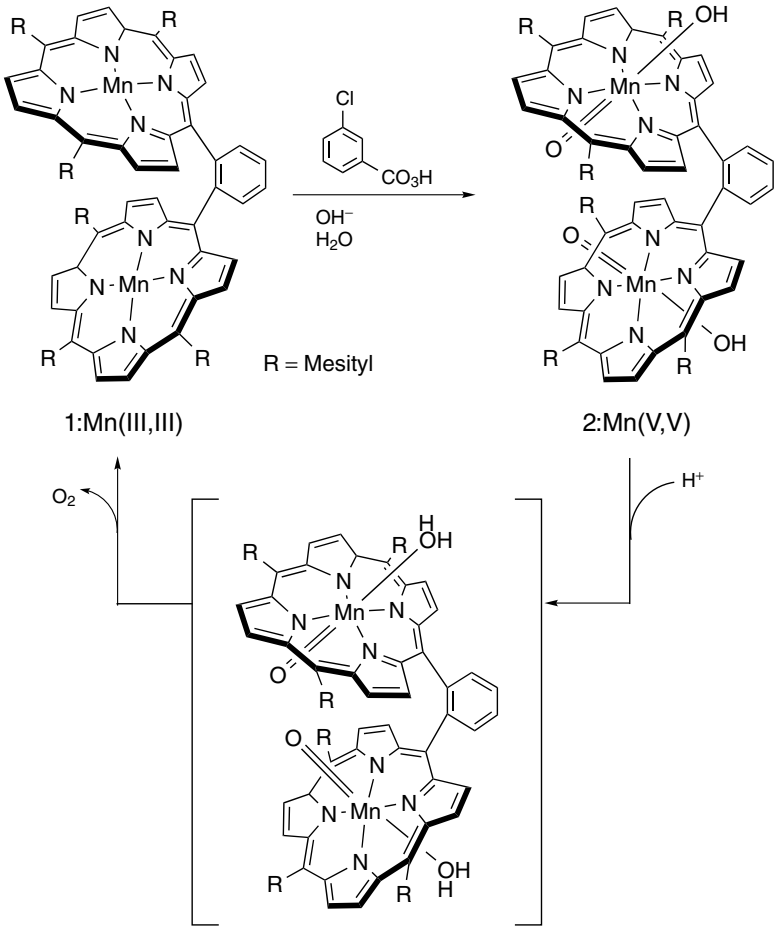

Figure 11 Structure of Mn_2-dimeric porphyrin complex (**1**) and a reaction pathway for O_2 formation through a dimanganyl (V,V) species (**2**)

10.2 Dimanganese(IV,V) Oxo Complexes

Although several examples of complexes containing the $[Mn_2O_2]^{n+}$ core type have been studied, only one has been found to catalyze O_2 evolution in water. The complex $[(terpy)(H_2O)Mn^{III}(\mu\text{-}O)_2Mn^{IV}(OH_2)(terpy)]^{3+}$ contains the tridentate terpyridine ligand that coordinates to three meridional sites on Mn and thus positions the two terminal aquo ligands trans to the μ-oxo bridges. The oxidation of this complex by SO_5^{2-} or OCl^- in water was shown to produce O_2 and permanganate.[52] Steady-state saturation kinetics were observed indicating the formation of an intermediate suggested to be a 1:1 precursor complex that decays to form a postulated manganyl intermediate $(H_2O)Mn^{III}(\mu\text{-}O)_2Mn^{V}{=}O$ that was not directly observed. The yields of labeled O_2 products were measured using ^{18}O-water by mass spectrometry. The authors show on the basis of the $m/z = 32$, 34, and 36 products that the oxidant SO_5^{2-} is directly responsible for forming O_2 by reacting with the kinetic intermediate which also reforms the starting catalyst $(H_2O)Mn^{III}(\mu\text{-}O)_2Mn^{IV}(OH_2)$. The yield of the m/z 34 and 36 products is argued to favor a second pathway in which (labelled) water or hydroxide is proposed to attack the kinetic intermediate to produce O_2 and a reduced $Mn^{II}Mn^{III}$ intermediate. The latter product is then recycled by reacting with excess oxidant to reform the original catalyst. This mechanism has been offered as indirect evidence for the possible presence of an analogous $Mn^{V}{=}O$ intermediate in PSII and for a heterolytic pathway for O–O bond formation. Additional evidence to identify the source of the m/z 34 and 36 products would be very helpful. The possibility of rapid exchange of oxygen atoms between water, the putative manganyl oxo and eventually into SO_5^{2-} could also explain the

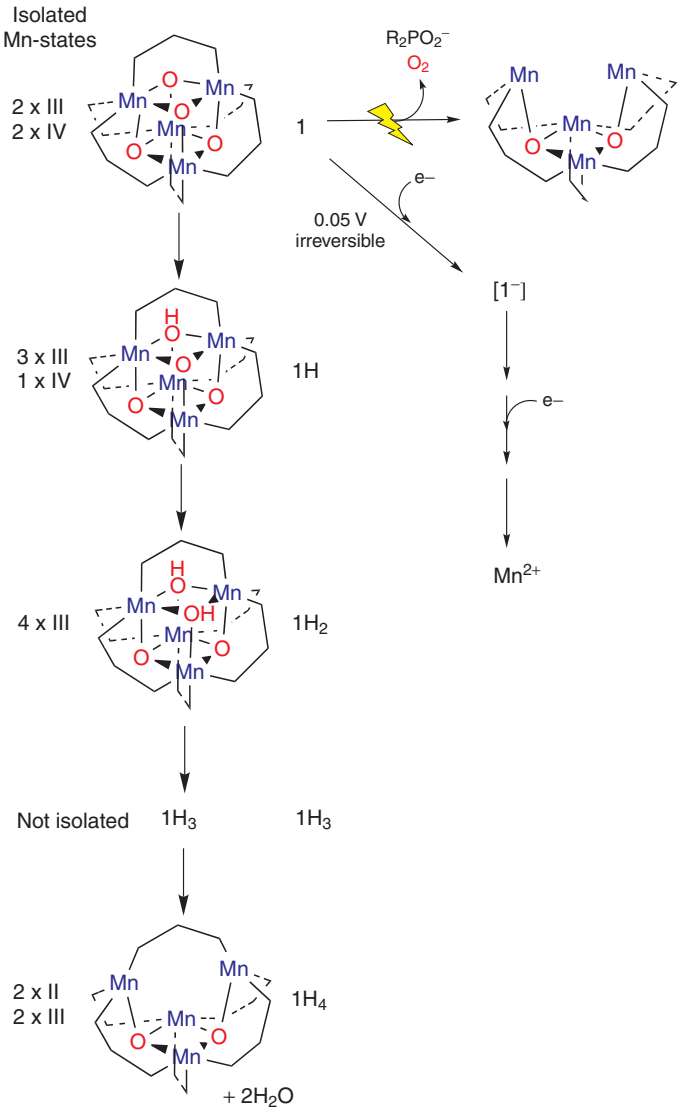

Figure 12 O_2 and water formation from $Mn_4O_4(Ph_2PO_2)_6$ complexes

isotope distribution of the O_2 product without invoking any water oxidation chemistry. The former exchange rate has been shown to be very rapid ($\sim 100\ s^{-1}$) in the case of the porphyrin class of $Mn^V{=}O$. Also, direct evidence to identify the formation of the manganyl intermediate and the use of innocent oxidants that do not deliver active oxygen atoms would also be very helpful in establishing the relevance of this chemistry to PSII-WOC. Recent studies using this same complex did not find evidence for the formation of O_2 in solution, but did find evidence that the complex forms a catalyst capable of low efficiency water splitting if adsorbed onto clays.[53] The active catalyst that produced O_2 was shown to involve two equivalents of the adsorbed dimanganese complex (e.g. 4Mn equiv.).

10.3 Mn_4O_4-Cubane-to-Mn_4O_2-Butterfly

A cubane/butterfly core rearrangement, represented by core type 12 (Figure 6), was proposed in an early hypothesis for the photosynthetic O_2 evolution step. The feasibility of this rearrangement has been demonstrated in a model cluster, as summarized in Figure 12.[26] The molecule $Mn_4O_4(Ph_2PO_2)_6$ can be synthesized from simple monomeric precursors (Mn^{2+} and MnO_4^-) in the presence of phosphinate anions which have long O–O' chelate distance that bridges between Mn ions. It contains a rare example of the symmetrical $[Mn_4O_4]^{6+}$ cubane core in the formal oxidation state Mn_4(2III, 2IV). The $[Mn_4O_4]^{6+}$ core has longer Mn–O bonds (by 0.15–0.2 Å) than the isoelectronic $[Mn_2O_2]^{3+}$ core complexes. By changing the type of phosphinate ligand, the core geometry changes from tetrahedral with equivalent Mn ions to C_2 with distinct Mn(IV) and Mn(III) sites.[54] Importantly, UV light absorption into a Mn–O charge transfer band efficiently releases an O_2 molecule in the gas phase together with one of the phosphinate chelates, leaving the intact cationic species $[Mn_4O_2(Ph_2PO_2)_5]^+$ (Mn_4O_2-butterfly core). This reaction proceeds with high quantum efficiency (>90%), is the only observable reaction channel (other than decay to the ground state), and is selective to the cubane core type (i.e. not observed for Mn_2O_2, Mn_2O, or Mn_3O_4 core complexes).[43] By comparing the isotopomers synthesized with $[Mn_4(^{18}O)_4]^{6+}$ and $[Mn_4(^{16}O)_4]^{6+}$ cores, the mechanism of O_2 formation was shown to proceed via intramolecular coupling of corner oxos. This chemistry illustrates that the cubane topology is intrinsically poised toward O_2 formation, in contrast to the $[Mn_2O_2]^{3+/4+}$ core complexes which do not release O_2 from the μ-oxos.

The mechanism of O–O bond formation has been supported by density functional calculations which show that, following removal of a phosphinate chelate, the resulting core is unstable towards O_2 release via a thermal pathway involving out of plane displacement of the oxygen atoms. This degree of freedom permits the oxygen atoms to approach one another in the transition state (ca 23–30 kcal mol^{-1}) in route to forming a peroxo-intermediate and O_2 release (F. De Angelis, R. Car, unpublished data). This appreciable activation barrier accounts for why the quantum yield is very low in solution owing to geminate recombination. The longer Mn–O bonds in the $[Mn_4O_4]^{6+}$ cubanes are weaker than those in $[Mn_2O_2]^{3+}$ core complexes, a feature which is believed responsible in part for their reactivity toward forming O_2.

Reduction of the parent cubane in solution using various H atom donors (organoamines and phenols) proceeds via successive intermediates differing by addition of H atoms to the corner oxos. A total of 4 H atoms can be delivered, but the isolated product is not the tetrakis μ-OH species $1H_4$, rather it is the dehydrated 'pinned butterfly' complex $Mn_4O_2(Ph_2PO_2)_6$ and two free water molecules.[55] The rate constants and H/D kinetic isotope effects were also examined. No further reduction below this oxidation state Mn(2II, 2III) is observed, indicating that the butterfly core topology is intrinsically resistant to further reduction.

The chemistry in Figure 12 gives direct experimental proof of the unique properties of the Mn_4O_2-butterfly/Mn_4O_4-cubane topology in the dehydrogenation of water to μ-oxos and coupling to form O_2. The possible relationship between this chemistry and the permissible mechanisms for biological water splitting is illustrated in Figures 9 and 10.

11 RELATED ARTICLES

Manganese: Inorganic & Coordination Chemistry; Manganese Proteins with Mono- & Dinuclear Sites.

12 REFERENCES

1. D. J. Des Marais, *Science*, 2000, **289**, 1703.
2. M. J. Russell and A. J. Hall, *Geochem. News*, 2002, **113**, 6.
3. G. C. Dismukes, V. V. Klimov, S. V. Baranov, Y. N. Kozlov, J. Dasgupta, and A. M. Tyryshkin, *Proc. Natl. Acad. Sci. U.S.A.*, 2001, **98**, 2170.
4. K. Sauer and V. K. Yachandra, *Proc. Natl. Acad. Sci. U.S.A.*, 2002, **99**, 8631.
5. R. E. Blankenship, 'Molecular Mechanisms of Photosynthesis', Blackwell Science, Oxford, 2002.
6. J. Nugent, ed. Photosynthetic Water Oxidation, B.B.A. Bioenergetics, vol. 1503, p. 1.
7. T. Wydrzynski and K. Satoh, eds. 'Photosystem II: The Water/Plastoquinone Oxido-Reductase in Photosynthesis' Springer, The Netherlands, 2005.
8. P. Joliot, *Photosynth. Res.*, 1993, **38**, 214.
9. G. M. Cheniae, *Photosynth. Res.*, 1993, **38**, 225.
10. C. G. Chen and G. M. Cheniae, *Plant Physiol.*, 1995, **108**, 87.
11. J. S. Vrettos, D. A. Stone, and G. W. Brudvig, *Biochemistry*, 2001, **40**, 7937.

12. G. M. Ananyev, L. Zaltsman, C. Vasko, and G. C. Dismukes, *Biochim. Biophys. Acta Bioenergetics*, 2001, **1503**, 52.
13. F. Rappaport and J. Lavergne, *Biochim. Biophys. Acta Bioenergetics*, 2001, **1503**, 246.
14. W. Junge, M. Haumann, R. Ahlbrink, A. Y. Mulkidjanian, and J. Clausen, *Philos. Trans. R. Soc. Lond, Ser. B Biol. Sci.*, 2002, **357**, 1407.
15. K. Olesen and L. E. Andreasson, *Biochemistry*, 2003, **42**, 2025.
16. G. Renger, *Biochim. Biophys. Acta Bioenergetics*, 2001, **1503**, 210.
17. W. Hillier and T. Wydrzynski, *Biochim. Biophys. Acta Bioenergetics*, 2001, **1503**, 197.
18. G. Hendry and W. T. Wydrzynski, *Biochemistry*, 2003, **42**, 6209.
19. A. Zouni, H.-T. Witt, J. Kern, P. Fromme, N. Krauss, W. Saenger, and P. Orth, *Nature*, 2001, **409**, 739.
20. N. Kamiya and J.-R. Shen, *Proc. Natl. Acad. Sci. U.S.A.*, 2003, **100**, 98.
21. K. N. Ferreira, T. M. Iverson, K. Maghlaoui, J. Barber, and S. Iwata, *Science*, 2004, **303**, 1831.
22. T. G. Carrell, A. Tyryshkin, and G. C. Dismukes, *J. Biol. Inorg. Chem.*, 2002, **7**, 2.
23. B. A. Diner and F. Rappaport, *Ann. Rev. Plant Biol.*, 2002, **52**, 551.
24. R. Debus, *Biochim. Biophys. Acta Bioenergetics*, 2001, **1503**, 164.
25. J. H. Robblee, R. M. Cinco, and V. K. Yachandra, *Biochim. Biophys. Acta Bioenergetics*, 2001, **1503**, 7.
26. W. Ruettinger, M. Yagi, K. Wolf, S. Bernasek, and G. C. Dismukes, *J. Am. Chem. Soc.*, 2000, **122**, 10353.
27. R. Debus, ed. The Catalytic Manganese Cluster–Protein Ligation, in 'Photosystem II: The Water/Plastoquinone Oxido-Reductase in Photosynthesis', eds. T. Wydrzynski and K. Satoh, Springer, The Netherlands, 2005, Chap. 11.
28. B. A. Diner, *Biochim. Biophys. Acta Bioenergetics*, 2001, **1503**, 147.
29. B. A. Diner, *Meth. Enzymol.*, 1998, **297**, 337.
30. J. Dasgupta, R. T. van Willigen, and G. C. Dismukes, *Physical Chem. Chem. Phys.*, 2004, **6**, 4793.
31. C. Rosenberg, J. Christian, T. M. Bricker, and C. Putnam-Evans, *Biochemistry*, 1999, **38**, 15994.
32. M. Knoepfle, T. M. Bricker, and C. Putnam-Evans, *Biochemistry*, 1999, **38**, 1582.
33. K. Hasegawa, T.-A. Ono, Y. Inoue and M. Kusunoki, *Bull. Chem. Soc. Jpn.*, 2000, **72**, 1013.
34. J. M. Peloquin and R. D. Britt, *Biochim. Biophys. Acta Bioenergetics*, 2001, **1503**, 96.
35. D. Kuzek and R. J. Pace, *Biochim. Biophys. Acta Bioenergetics*, 2001, **1503**, 123.
36. R. D. Britt, J. M. Peloquin, and K. A. Campbell, *Ann. Rev. Biophys. Biomol. Struct.*, 2000, **29**, 463.
37. M. Karge, K.-D. Irrgang, and G. Renger, *Biochemistry*, 1997, **36**, 8904.
38. K. L. Westphal, C. Tommos, R. I. Cukier, and G. T. Babcock, *Curr. Opin. Plant Biol.*, 2000, **3**, 236.
39. G. Renger, G. Christen, M. Karge, H.-J. Eckert, and K.-D. Irrgang, *J. Biol. Inorg. Chem.*, 1998, **3**, 360.
40. R. Fiege, W. Zweygart, R. Bittl, N. Adir, G. Renger, and W. Lubitz, *Photosynth. Res.*, 1996, **48**, 227.
41. X. S. Tang, M. Sivaraja, and G. C. Dismukes, *J. Am. Chem. Soc.*, 1993, **115**, 2382.
42. C. Aznar and R. Britt, *Philos. Trans. R. Soc. London, Ser. B*, 2002, **357**, 1359.
43. M. Yagi and M. Kaneko, *Chem. Rev.*, 2001, **101**, 21.
44. J. S. Vrettos and G. W. Brudvig, *Philos. Trans. R. Soc. Lond. B Biol. Sci.*, 2002, **357**(1426), 1395.
45. P. E. M. Siegbahn, *Curr. Opin. Chem. Biol.*, 2002, **6**, 227.
46. V. V. Klimov and S. V. Baranov, *Biochim. Biophys. Acta Bioenergetics*, 2001, **1503**, 187.
47. D. E. Richardson, H. Yao, K. M. Frank, and D. A. Bennett, *J. Am. Chem. Soc.*, 2000, **122**, 1729.
48. K. L. Westphal, N. Lydakis-Simantiris, R. I. Cukier, and G. T. Babcock, *Biochemistry*, 2000, **39**, 16220.
49. S. Baranov, A. Tyryshkin, D. Katz, G. Ananyev, V. Klimov, and G. Dismukes, *Biochemistry*, 2004, **43**, 2070.
50. W. Ruettinger and G. C. Dismukes, *Chem. Rev.*, 1997, **97**, 1.
51. R. Manchandra, G. W. Brudvig, and R. H. Crabtree, *Coord. Chem. Rev.*, 1995, **144**, 1.
52. J. Limburg, J. S. Vrettos, H. Chen, J. C. de Paula, R. H. Crabtree, and G. W. Brudvig, *J. Am. Chem. Soc.*, 2001, **123**, 423.
53. M. Yagi and K. Narita, *J. Am. Chem. Soc.*, 2004, **126**, 8084.
54. J.-Z. Wu, E. Selitto, G. Yap, J. Sheats, and G. C. Dismukes, 2004, vol. 43, 5795.
55. M. Maneiro, W. F. Ruettinger, E. Bourles, G. McLendon, and G. C. Dismukes, *Proc. Natl. Acad. Sci. U.S.A.*, 2003, **100**, 3703.

Acknowledgments

We thank M. Yagi and R. Debus for preprints of their work and W. Ruettinger for assistance with figures. RvW acknowledges support by Princeton University, Leiden University, and the Human Frontiers Science Program (RG-P0029-2002). Research in the authors' laboratory has been supported by the National Institutes of Health (GM-39932).